

A high-precision formula for mixed-order polygon elements based on SBFEM

Kai Chen, Degao Zou^{*}, Jingmao Liu, Yue Zhuo

The State Key Laboratory of Coastal and Offshore Engineering, Dalian University of Technology, Dalian, Liaoning 116024, China
School of Hydraulic Engineering, Dalian University of Technology, Dalian, Liaoning 116024, China

ARTICLE INFO

Keywords:

Scaled boundary finite element method
Mixed-order interpolation
Bending problems

ABSTRACT

A satisfactory balance between solution precision and computational efficiency can be achieved via mixed-order elements, however, the generality and robustness of commonly used methods can be further optimized. In this paper, a flexible and versatile mixed-order analysis method is developed based on Scaled Boundary Finite Element Method (SBFEM) theory, wherein one-dimensional linear and quadratic functions are combined to interpolate circular boundaries. The applicability and accuracy of the proposed method for different problems are explored and compared, and good accuracy and tolerance of element distortion performance are revealed. Moreover, compared with the quadratic element, computational efforts can be reduced considerably, enabling efficiency to be enhanced. Additionally, a polygon mixed-order formula can be directly derived, benefiting from the advantages of the SBFEM, wherein stronger universalities are rendered. In summary, the proposed method improves the flexibility and robustness of the mixed-order cells, and distinctive superiorities are revealed, providing an alternative option for the efficient and high-precision numerical analysis of vital structures.

1. Introduction

Component bending problems are extremely common in real life, such as airfoil bending. Additionally, tower cranes are typical cantilever beams with a bending deformation pattern. Portal crane and bridges are equivalent to simply supported beams. As the deformation gradient in partial areas is steep, higher accuracy requirements for computational methods are inevitable. However, a larger deformation gradient can be allowed in most of the other domains; correspondingly, the accuracy of computation methods can be relaxed without affecting the results. From the perspective of finite element analysis, the aforementioned problems evolve into a contradiction that a good balance between computational efficiency and solution accuracy is difficult to achieve. That is, to obtain the exact solution of a component, high-precision cells or a denser mesh discretization scheme must be globally adopted. However, these configurations are not essential for the majority of computational domains, which means that unnecessary effort is being carried out. Therefore, how to optimize the balance between accuracy and efficiency has been a hot research direction and a desirable simulation goal continuously pursued by researchers in engineering computational mechanics worldwide.

Over the years, research studies on numerical analysis methods have been sustainably pushed forward. For different problems, suitable approaches have been proposed, and good application performance has been achieved, such as high-precision nonconforming elements (Droniou et al., 2021), the scaled boundary finite element method (SBFEM) (Chen et al., 2021; Song, 2009), higher-order cells (Vu-Huu et al., 2019), flexible serendipity elements (Utku, 1999), the virtual element method (Zhao et al., 2016), multi-scale analysis method (Guo et al., 2021; Zhao and Zhao, 2019; 2020), and hydraulic-force coupled analysis (Chen et al., 2021). Among them, combining different order elements for local refinement analysis, e.g., a linear to a quadratic element, is an effective way to achieve a desirable balance between computational accuracy and efficiency. As the literature shows, this inspiration has been mainly performed via two methods (Utku, 1999). One method is that the transition elements with different numbers of nodes through the boundaries can be formulated. The constraint equations introduced can be defined as the second method, wherein the requirement of displacement coordination and continuity between adjacent elements must be strictly guaranteed (Carey et al., 1987; Gopalakrishnan et al., 1990; Reddy, 2004).

Isoparametric elements are the most commonly used and

^{*} Corresponding author at: The State Key Laboratory of Coastal and Offshore Engineering, Dalian University of Technology, Dalian, Liaoning 116024, China.
E-mail address: zoudegao@dlut.edu.cn (D. Zou).

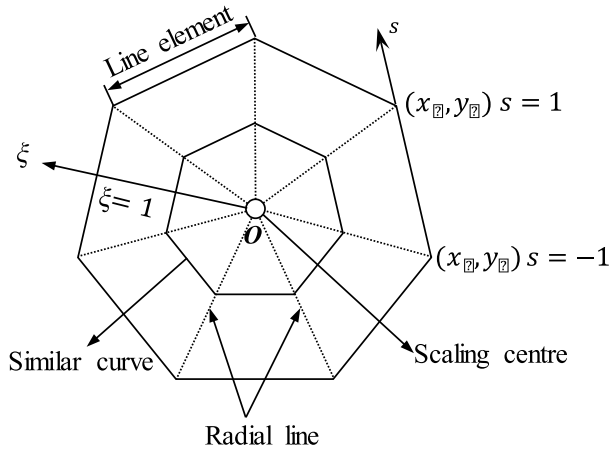


Fig. 1. Polygon representation of the scaled boundary finite element method.

straightforward method in local refinement analysis for the purpose of achieving transition and constraint balance between adjacent elements. According to the existing literature, flexible serendipity elements are highly recommended in simulations. These elements have access to the configuration of different orders on each side in the element, such as linear, quadratic or cubic, which can be allowed simultaneously. Notably, when the order of each side is identical, the element can degenerate into conventional isoparametric elements, such as 4-node quadrilateral and 8-node quadrilateral elements. However, it is worth noting that in the early research literature (Çitipitioglu, 1983; Gopalakrishnan et al., 1990; Nicolas and Citipitioglu, 1977), the serendipity elements adopt the idea of isoparametric transformation, wherein a mapping relationship between parent elements and the physical domain must be established. Under such conditions, the nodes on the element edges in the physical domain must be fixedly mapped to the parent elements. If the node position deviates in the physical domain, then the interpolation polynomial in the parent elements will be distorted, which is called the node mapping distortion (Utku, 1999). To avoid this deficiency, related improvements have been made, and researchers have proposed more flexible parent elements (adjustable edge node positions) (Utku, 1999). Recently, this method has also been continuously improved by researchers, and different forms of optimization derivation have been proposed, such as in (Wriggers et al., 2021). However, the expression of this method is more complex than the isoparametric elements, and extra optimization space for its simplicity and universality can be further enhanced. In consideration of the above characteristics, theoretical improvements and mechanism research have been the primary focus for the method, while the applications of engineering structures are rarely involved.

The scaled boundary finite element method (SBFEM) is a semi-analytic method proposed by Wolf and Song (Song and Wolf, 1997). Compared to conventional methods, some remarkable advantages are revealed with SBFEM: the calculation can be reduced by one-dimension, polygonal cells can be directly formulated, numerical implementation is straightforward and so on; therefore, the method has received much attention from researchers. Some representative research studies are listed as follows. Using the SBFEM, a perfect nanographene sheet or cracked sheet was simulated for the first time (Honarmand and Moradi, 2018). The theory of the SBFEM was systematically established as a general numerical procedure, providing the reader with sound knowledge to expand the applications of this method to a broader scope (Song, 2018). Li et al. (2018) developed a unified and efficient simulation technique based on the scaled boundary finite element method for transient structural-acoustic problems in two dimensions. Zou et al. presented a polyhedral scaled boundary FEM (SBFEM) to investigate the

three-dimensional seismic response of saturated porous media (Zou et al., 2019) and extended the method to the complex element technique (Zou et al., 2017) and geotechnical nonlinear analysis (Chen et al., 2017, 2018a, 2018b, 2019). Three alternative approaches, namely, the extended/generalized finite element method (XFEM/GFEM), the scaled boundary finite element method (SBFEM) and phase field methods, were surveyed and compared in the context of linear elastic fracture mechanics (LEFM). The objective of (Egger et al., 2019) was to provide a critical literature review, emphasizing the mathematical, conceptual and implementation particularities that lead to the specific advantages and disadvantages of each method, as well as to offer numerical examples that help illustrate these features. Various numerical examples have been presented to demonstrate the accuracy, efficiency and capability of this approach for analyzing acoustic problems with complex geometries (Liu et al., 2019). The evanescent wave theory of an infinite length cylindrical shell was adopted to theoretically analyze the decay characteristic of evanescent waves in the near field (Huang et al., 2020). In (Li et al., 2020), an efficient modeling technique was developed based on the scaled boundary finite element method for transient vibro-acoustic analysis of plates and shells. Other influential work includes combining the SBFEM with Cosserat theory to improve analysis accuracy (Chen et al. 2021a, 2021b); Liu et al. (Liu et al., 2020, 2022) studied the static and dynamic responses of piezoelectric laminated and sandwich cylindrical shells based on the SBFEM. Moreover, these researchers presented a three-dimensional semi-analytical solution for bending and vibration analyses of functionally graded material beams and plate structures by using the SBFEM (Liu et al., 2021a, 2021b); crack propagation (Ooi et al., 2013, 2016) (momentous and novel alternative approaches to failure analysis), transient wave propagation (Chen et al., 2014), soil-structure interactions (Birk and Behnke, 2012), thermology (Li et al., 2017), fluid-solid coupling (Xu et al., 2016), and concrete fracture based on in-situ X-ray (Huang et al., 2015; Yang et al., 2017), and the analysis of seismic wave propagation problems (Gravenkamp et al., 2017). From the aspect of theoretical construction, the mixed-order element formula can be automatically achieved; that is, each boundary can be selected for the interpolation of one-dimensional line elements with different orders. More importantly, the whole process does not require any modification of the original formulation; therefore, the difficulty of numerical development is unaffected.

To further enhance the simplicity and universality of existing mixed-order elements, the contradiction between the solution accuracy and computational efficiency in conventional analysis can be optimized. In this paper, based on the theory of the SBFEM, a flexible and general mixed-order hybrid element is developed, wherein one-dimensional linear and quadratic functions are adopted to interpolate the circumferential boundaries. Subsequently, the applicability and accuracy of the proposed method for different problems are discussed and compared.

2. SBFEM formulation for mixed-order elements

2.1. Circumferential interpolation

After decades of development, the scaled boundary finite element method has been promoted and applied by researchers, and abundant literature can be available. Therefore, only some key equations are expressed herein. A representative polygon element calculated via SBFEM is illustrated in Fig. 1. The circumferential boundaries can be discretized using a one-dimensional or quadratic line element, and the local coordinate system (ξ, s) is defined, learning from the FEM. The radial coordinate ξ is taken as 0 at scale center O and becomes 1.0 at the boundary; similarly, the value of circumferential coordinates is specified as $-1 \leq s \leq 1$. In this manner, the coordinates of any point on the line element can be calculated by interpolation of the node coordinates, as given in Eqs. (1) and (2).

$$\mathbf{x}_b(s) = \mathbf{N}(s)\mathbf{x}_b \quad (1)$$

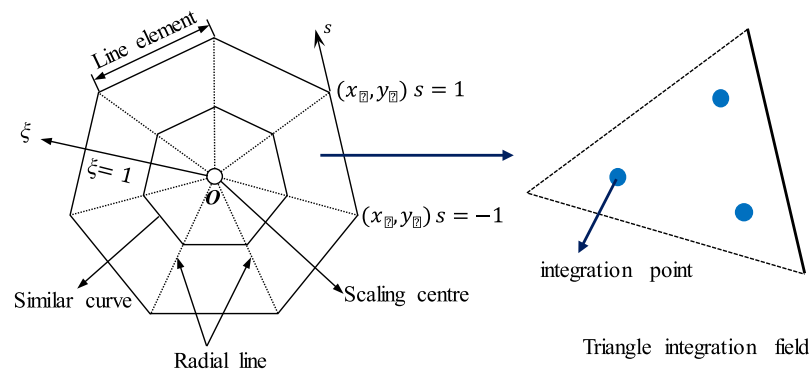
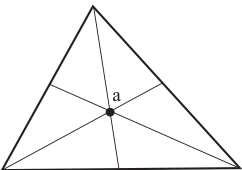
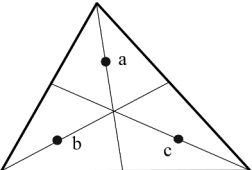
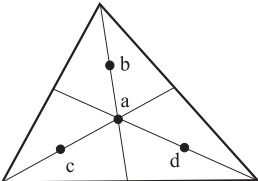
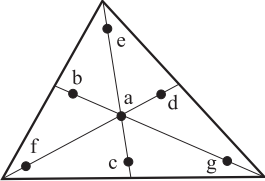


Fig. 2. Illustration of sector integration in the polygonal domain.

Table 1
Information on the Hammer integration points in the triangular sector domain.

Accuracy	Location	Error	Points	Coordinates	Weight*
Linear		$R = O(h^2)$	a	$\frac{1}{3}, \frac{1}{3}, \frac{1}{3}$	1
Quadratic		$R = O(h^3)$	a	$\frac{2}{3}, \frac{1}{6}, \frac{1}{6}$	$\frac{1}{3}$
			b	$\frac{1}{6}, \frac{2}{3}, \frac{1}{6}$	$\frac{1}{3}$
			c	$\frac{1}{6}, \frac{1}{6}, \frac{2}{3}$	$\frac{1}{3}$
Third order		$R = O(h^4)$	a	$\frac{1}{3}, \frac{1}{3}, \frac{1}{3}$	$-\frac{27}{48}$
			b	0.6, 0.2, 0.2	25/48
			c	0.2, 0.6, 0.2	
			d	0.2, 0.2, 0.6	
Fifth order		$R = O(h^6)$	a	$\frac{1}{3}, \frac{1}{3}, \frac{1}{3}$	0.225
			b	$\alpha_1, \beta_1, \beta_1$	0.1323941527
			c	$\beta_1, \alpha_1, \beta_1$	
			d	$\beta_1, \beta_1, \alpha_1$	
			e	$\alpha_2, \beta_2, \beta_2$	0.1259391805
			f	$\beta_2, \alpha_2, \beta_2$	
			g	$\beta_2, \beta_2, \alpha_2$	
				$\alpha_1 = 0.0597158717, \alpha_2 = 0.7974269853,$ $\beta_1 = 0.4701420641, \beta_2 = 0.1012865073$	

* Since the integration domain of the triangle involves the variables themselves, the sum of the weights should be equal to 1/2, so the weights listed in the table should be multiplied by 1/2.

Table 2
Description of element type referred in the paper.

Abbreviation	Description of the elements
Quad4 (Provided by Commercial Software ANSYS)	Isoparametric element with 4 nodes
Quad8 (Provided by Commercial Software ANSYS)	Isoparametric element with 8 nodes
QM6(Aylor et al., 2010)	Non-conforming element (Taylor, Wilson). It is possible to 'repair' the defect in the element (Q^6) by examining the patch test and correcting the defective terms. The element which is produced is herein called QM ⁶ and degenerates to the Q^6 element whenever it is a parallelogram
SBFEM-L	Scaled Boundary Finite Element Method via boundary line integration with 2 gauss points in the circumferential direction
SBFEM-Q	Scaled Boundary Finite Element Method via boundary linear integration with 3 gauss points in the circumferential direction
SBFEM-C (Presented method in this paper)	Scaled Boundary Finite Element Method via boundary linear integration with 2 or 3 gauss points in the circumferential direction

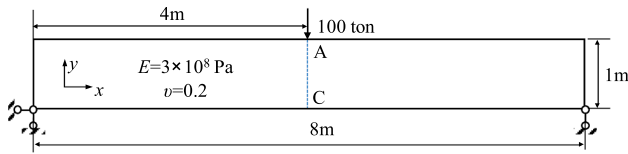
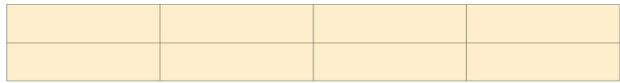
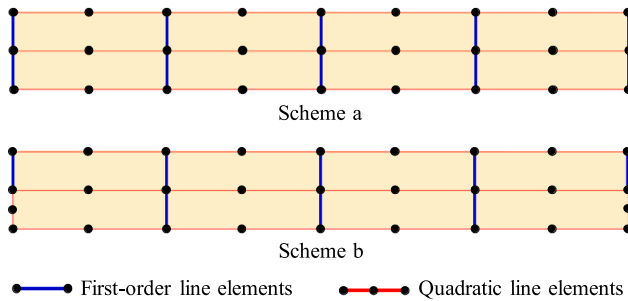


Fig. 3. Geometry description of the simply supported beam.



(a) Traditional mesh



(b) Mixed-order mesh

Fig. 4. Schematic of mesh discretization for the supported beam.

Table 3
Deflection of point C for the supported beam.

Method	Quad4: ANSYS	SBFEM-L	Quad8: ANSYS	SBFEM-Q	SBFEM-C: Presented	
					Scheme a	Scheme b
D_c / m	0.162	0.167	0.420	0.427	0.419	0.421
(Deviation)	(62.0 %)	(60.9 %)	(1.6 %)	(0.07 %)	(1.8 %)	(1.3 %)
Degrees of freedom	30	74	54	58		

$$y_b(s) = N(s)y_b \quad (2)$$

$$N(s) = [N_1(s), N_2(s), N_3(s), \dots, N_m(s)] \quad (3)$$

$$N_1(s) = (1-s)/2, N_2(s) = (1+s)/2 \quad (4)$$

$$N_1(s) = s(1-s)/2, N_2(s) = 1-s^2, N_3(s) = s(1+s)/2 \quad (5)$$

where $N(s)$ is the shape function of a line element containing m nodes, with unlimited order in Eq. (3). In this paper, two interpolation models are used, i.e., first-order and quadratic elements, and the expressions are given in Eq. (4) and Eq. (5). With the advantage of scaled boundary finite elements, the use of boundary cells of different orders does not affect the derivation of subsequent equations. After obtaining the boundary coordinates, the coordinates of any point in the computational domain can be obtained by scaling the radial coordinate ξ , as provided in Eqs. (6) and (7).

$$x(\xi, s) = \xi N(s)x_b \quad (6)$$

$$y(\xi, s) = \xi N(s)y_b \quad (7)$$

The boundary elements adopt isoparametric interpolation and assume the existence of a unique interpolation function $u(\xi)$ in the radial direction. Then, the displacement of any point in a sector domain, which is obtained by connecting the scale center and the annular boundary, can be calculated by the node interpolation function. The specific calculation formula is provided in Eq. (8).

$$u(\xi, s) = N_u(s)u(\xi) \quad (8)$$

where $N_u(s)$ is the interpolation function of the boundary line element. $u(\xi)$ can be obtained by solving the SBFEM equilibrium equation, whose expression is given in Eq. (9).

$$E_0 \xi^2 u(\xi)_{\xi\xi} + (E_0 - E_1 + E_1^T) \xi u(\xi)_{\xi} - E_2 u(\xi) + F(\xi) = 0 \quad (9)$$

Eq. (9) is a second-order inhomogeneous partial differential equation with respect to ξ , where E_i ($i = 0, 1, 2$) is a matrix of coefficients related only to material properties and geometry, and the expression is given in Eq. (10).

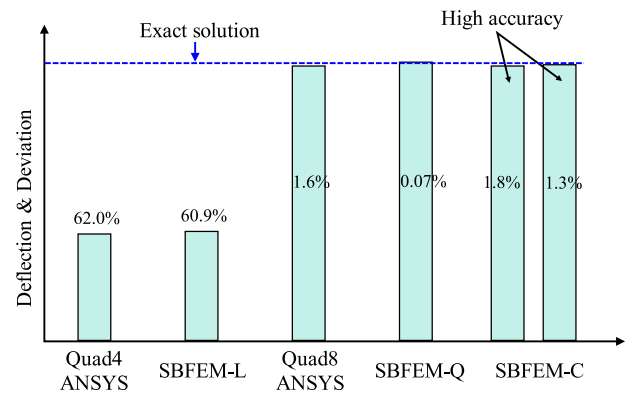
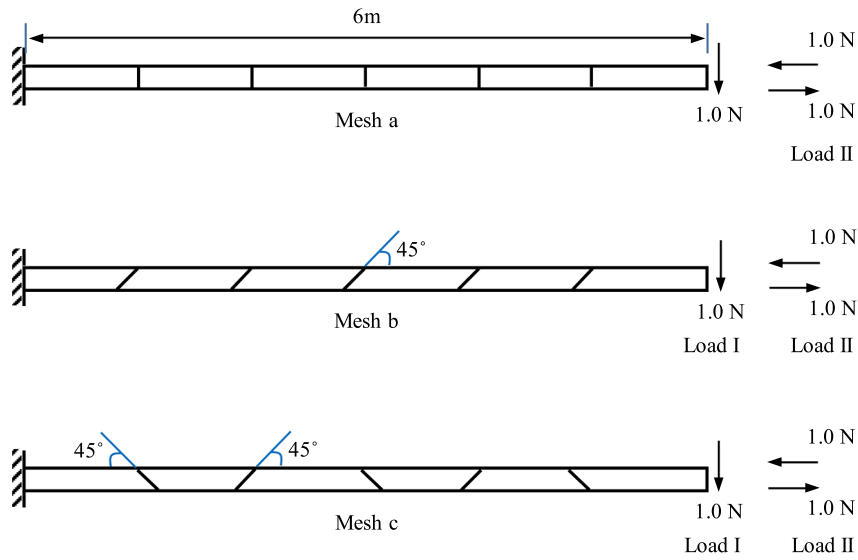


Fig. 5. Illustration of deflection for different approaches.



8Fig. 6. Diagram of the MacNeal beam.

Table 4
Normalized tip displacements for the MacNeal beam problem.

Elements type	Load I condition			Load II condition		
	Mesh a	Mesh b	Mesh c	Mesh a	Mesh b	Mesh c
Quad4: ANSYS	0.904	0.080	0.071	–	–	–
QM ⁶ (Aylor et al., 2010)	0.993	0.623	0.044	1.000	0.722	0.037
Quad8: ANSYS	0.994	0.978	0.909	1.000	0.994	0.932
SBFEM-C	0.995	0.989	0.907	1.000	1.000	1.000
(Presented)						
Exact Solutions	1.000*			1.000**		

Notes:

* Reference value is -0.1081 ,

** Reference value is -0.0054 .

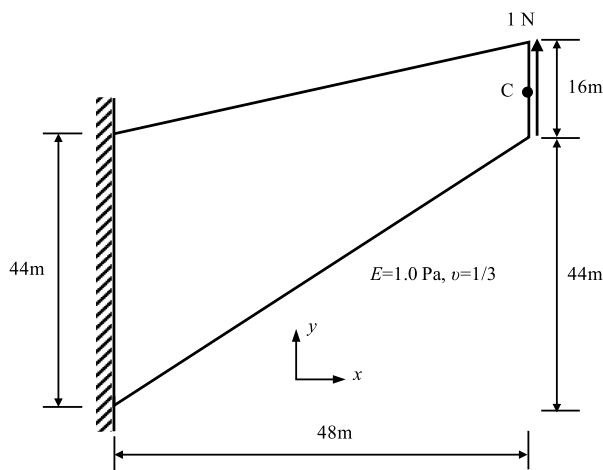


Fig. 7. Schematic of the cook's beam.

$$E_1 = \int_{-1}^{+1} \mathbf{B}_2^T(s) \mathbf{D} \mathbf{B}_1(s) |\mathbf{J}(s)| ds \quad (10b)$$

$$E_2 = \int_{-1}^{+1} \mathbf{B}_2^T(s) \mathbf{D} \mathbf{B}_2(s) |\mathbf{J}(s)| ds \quad (10c)$$

where \mathbf{D} is the material constitutive matrix and $|\mathbf{J}(s)|$ is the Jacobian matrix determinant. $\mathbf{B}_1(s)$ and $\mathbf{B}_2(s)$ are the strain displacement transformation matrices, and the expressions are provided as follows:

$$\mathbf{B}_1(s) = \frac{1}{|\mathbf{J}(s)|} \begin{bmatrix} \mathbf{y}_b(s)_{,s} & 0 \\ 0 & -\mathbf{x}_b(s)_{,s} \\ -\mathbf{x}_b(s)_{,s} & \mathbf{y}_b(s)_{,s} \end{bmatrix} \mathbf{N}_u(s) \quad (11a)$$

$$\mathbf{B}_2(s) = \frac{1}{|\mathbf{J}(s)|} \begin{bmatrix} -\mathbf{y}_b(s)_{,s} & 0 \\ 0 & \mathbf{x}_b(s)_{,s} \\ \mathbf{x}_b(s)_{,s} & -\mathbf{y}_b(s)_{,s} \end{bmatrix} \mathbf{N}_u(s) \quad (11b)$$

$\mathbf{F}(\xi)$ in Eq. (9) is the external load vector. When $\mathbf{F}(\xi) = 0$, the control equation can be converted to a second-order homogeneous partial differential equation, and then the variable $\mathbf{X}(\xi)$ is introduced. The equation can be converted to a first-order homogeneous differential equation; see Eqs. (12) and (13).

$$\mathbf{X}(\xi) = \begin{Bmatrix} \mathbf{u}(\xi) \\ \mathbf{q}(\xi) \end{Bmatrix} \quad (12)$$

$$\xi \mathbf{X}(\xi)_{,\xi} = -\mathbf{Z} \mathbf{X}(\xi) \quad (13)$$

where \mathbf{Z} is the Hamiltonian matrix, the expression of which is given in (14), and $\mathbf{q}(\xi)$ is the internal nodal force vector corresponding to $\mathbf{u}(\xi)$.

$$\mathbf{Z} = \begin{bmatrix} \mathbf{E}_0^{-1} \mathbf{E}_1^T & -\mathbf{E}_0^{-1} \\ \mathbf{E}_1 \mathbf{E}_0^{-1} \mathbf{E}_1^T - \mathbf{E}_2 & -\mathbf{E}_1 \mathbf{E}_0^{-1} \end{bmatrix} \quad (14)$$

By performing an eigenvalue decomposition of the Hamiltonian matrix \mathbf{Z} , the relation of Eq. (15) is obtained for each polygon element.

$$\mathbf{Z} \begin{bmatrix} \boldsymbol{\psi}_u \\ \boldsymbol{\psi}_q \end{bmatrix} = \begin{bmatrix} \boldsymbol{\psi}_u \\ \boldsymbol{\psi}_q \end{bmatrix} \mathbf{S}_n \quad (15)$$

where \mathbf{S}_n is the diagonal matrix consisting of the real part of the negative eigenvalues of the \mathbf{Z} matrix, $\boldsymbol{\psi}_u$ and $\boldsymbol{\psi}_q$ are the corresponding transformation matrices of the displacement and stress modes, respectively,

$$E_0 = \int_{-1}^{+1} \mathbf{B}_1^T(s) \mathbf{D} \mathbf{B}_1(s) |\mathbf{J}(s)| ds \quad (10a)$$

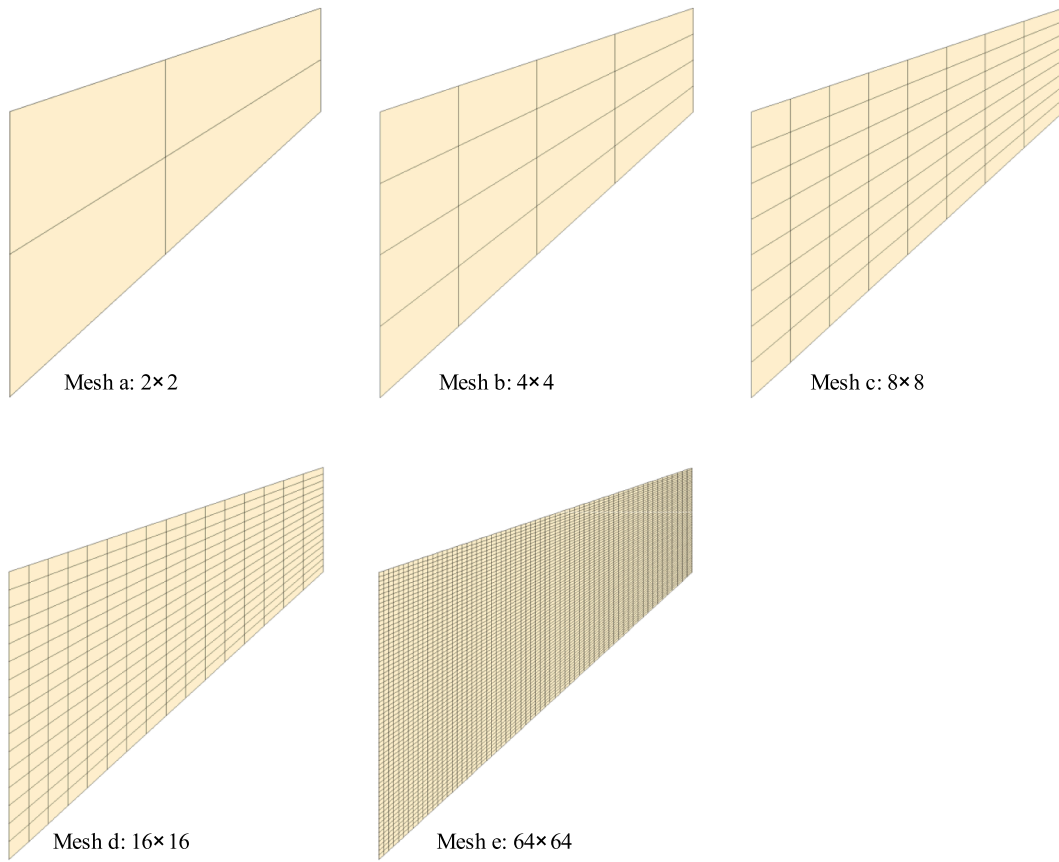


Fig. 8. Different meshes of the cook's beam.

Table 5
Deflection of point C for the cook's beam.

Mesh	D_C / m			
	Quad4: ANSYS	SBFEM-L	Quad8: ANSYS	SBFEM-Q
2×2	11.01	12.53	22.53	23.19
4×4	17.72	18.94	23.20	23.26
8×8	21.51	21.97	23.28	23.30
16×16	22.81	22.95	23.29	23.30
64×64	23.27	23.28	23.30	23.30

and the solution of Eq. (9) is Eq. (16) for the polygonal cell.

$$\begin{aligned} \mathbf{u}(\xi) &= \boldsymbol{\Psi}_u \xi^{-S_n} \mathbf{c}_n \\ \mathbf{q}(\xi) &= \boldsymbol{\Psi}_q \xi^{-S_n} \mathbf{c}_n \end{aligned} \quad (16)$$

where \mathbf{c}_n is the integration constant, which can be obtained from the nodal displacement \mathbf{u}_b on the polygon cell boundary; see Eq. (17). Thus far, the polygonal cell shape function $\Phi(\xi, s)$ can be determined, and the expression is given in Eq. (18).

$$\mathbf{c}_n = \boldsymbol{\Psi}_u^{-1} \mathbf{u}_b \quad (17)$$

$$\Phi(\xi, s) = N_u(s) \boldsymbol{\Psi}_u \xi^{-S_n} \boldsymbol{\Psi}_u^{-1} \quad (18)$$

In SBFEM theory, Wolf (2003) gives the strain expression (19a), and by substituting the displacement $\mathbf{u}(\xi)$, the strain-displacement transformation matrix $\mathbf{B}(\xi, s)$ can be obtained; see Eqs. (19b) and (19c).

$$\boldsymbol{\varepsilon}(\xi, s) = \mathbf{B}_1(s) \mathbf{u}(\xi)_{,\xi} + \xi^{-1} \mathbf{B}_2(s) \mathbf{u}(\xi) \quad (19a)$$

$$\boldsymbol{\varepsilon}(\xi, s) = ([\mathbf{B}_1(s) \boldsymbol{\Psi}_u [-S_n] + \mathbf{B}_2(s) \boldsymbol{\Psi}_u] \xi^{-S_n - I} \boldsymbol{\Psi}_u^{-1}) \mathbf{u}_b \quad (19b)$$

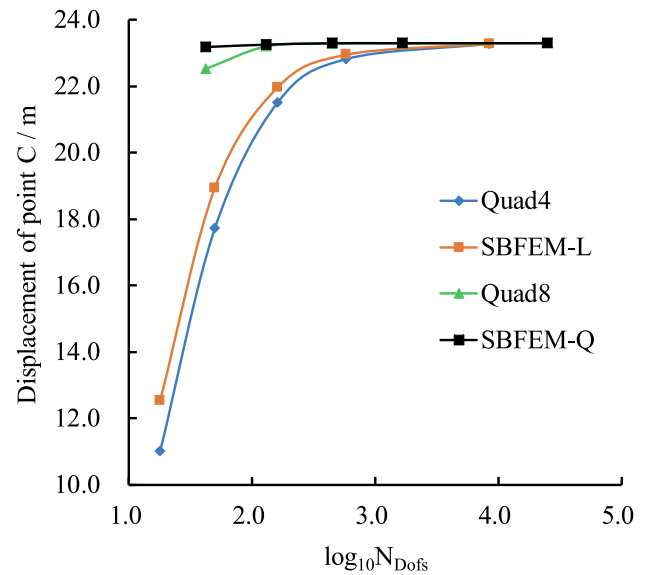


Fig. 9. Displacement versus degree of freedom curve using different elements.

$$\mathbf{B}(\xi, s) = [\mathbf{B}_1(s) \boldsymbol{\Psi}_u [-S_n] + \mathbf{B}_2(s) \boldsymbol{\Psi}_u] \xi^{-S_n - I} \boldsymbol{\Psi}_u^{-1} \quad (19c)$$

2.2. Integration within the sector domain

Numerical integration schemes for quadrilateral and triangular cells are prescribed in conventional finite element theory. For polygonal cells

Table 6
Degrees of freedom of the cook's beam.

Mesh	Degrees of freedom			
	Quad4	SBFEM-L	Quad8	SBFEM-Q
2×2	18	42		
4×4	50	130		
8×8	162	450		
16×16	578	1666		
64×64	8450	25,090		

with more than 4 sides, the numerical integration method of subdividing polygons is commonly used.

Based on this approach, the element can be dissected into multiple sector domains by connecting the scale center O and the circumferential boundary nodes. For example, Fig. 2 shows a typical heptagon, which can be divided into seven sectors. The problem of integration within the polygon cell domain can be solved by individually integrating each triangular sector domain in turn and then assembling the product variable by chunking the degrees of freedom.

In this paper, according to the triangular Hammer integration rule, three integration points are selected in each sector domain as an example to introduce, and the corresponding coordinates and weights are shown in Table 1. The researchers can select different integration points to construct different performances of the elements according to the actual needs.

According to the location of the area coordinates of the three integration points in each sector domain, the SBFEM local coordinates (ξ, s) corresponding to the integration points can be deduced as $(1/3, 0)$, $(5/6, -3/5)$, and $(5/6, 3/5)$, respectively. Through Eq. (11), $B_1(s)$ and $B_2(s)$ corresponding to the polygon domain can be calculated. Then, the polygonal element shape function and strain displacement transformation matrix can be derived by Eqs. (18) and (19c). Based on the above variables, the element stiffness matrix can be derived by Eq. (20), where the elastoplastic construction matrix D_{ep} is obtained by calling the materials construction module, and then the element values are calculated according to the offered block integration scheme. Finally, the overall stiffness matrix of the computational domain can be obtained by assembling in pieces according to the degrees of freedom.

$$\mathbf{K}_{ep} = \sum_{i=1}^{3n} \mathbf{B}^i(\xi, s) \mathbf{D}_{ep}^i \mathbf{B}^i(\xi, s) A_i \quad (20)$$

3. Numerical verification and application

This section explores the applicability of the developed method for different structural analyses, and the accuracy is compared with other methods. The element types referred in the paper are listed in Table 2. The computer software, GEODYNA7.0, integrates a variety of numerical analysis methods, such as SBFEM, constitutive models, and including the method offered in Table 2. And the software has been validated via

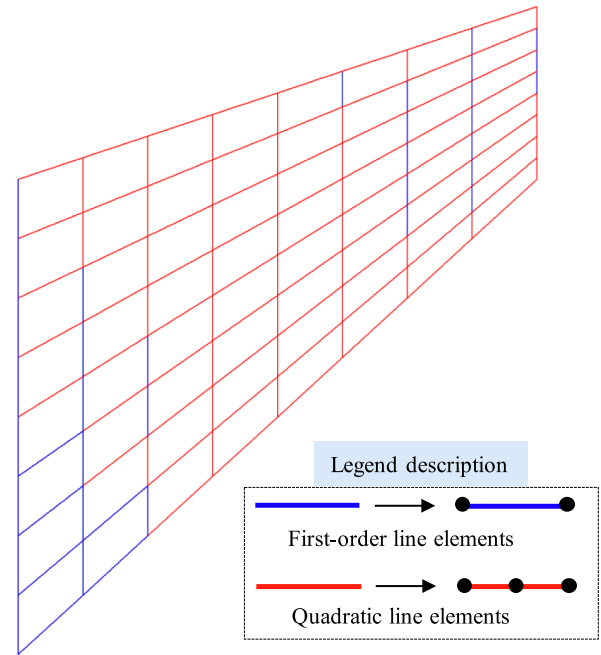


Fig. 11. Schematic of the assignment for order of the boundary line element.

Table 7
Statistics of the maximum displacement and degrees of freedom of SBFEM-C.

Deflection angle $\theta/^\circ$	D_c / m (Deviation)	Degrees of freedom	Reduction over quadratic cells / %
0.0	23.30	450	—
1.3	23.30	372	17.3
2.0	23.06 (1.0 %)	280	37.8
3.0	22.71 (2.5 %)	230	48.9
4.0	22.15 (4.9 %)	174	61.3

numerous benchmarks and engineering applications (Chen et al., 2017, 2018a, 2018b, 2019; Xu et al., 2015; Zou et al., 2017, 2019), is adopted for simulations in this study. And five examples of calculations are investigated, including four validations and one engineering application.

3.1. Verification of high accuracy

Fig. 3 shows the geometry of a simply supported beam, and the parameters and load information are also provided. The modulus $E = 3.0 \times 10^8$ Pa and Poisson's ratio $\nu = 0.2$. A concentrated load $F = 100$ ton at point A is applied at the top of the span. In this section, based on the

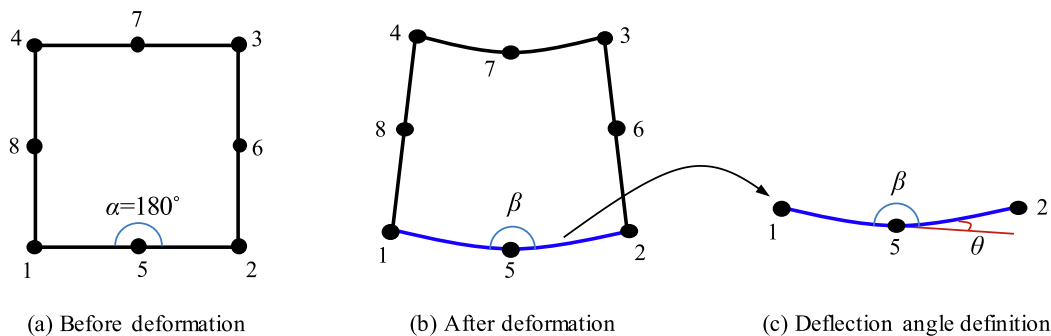


Fig. 10. Diagram of the deflection angle definition for quadratic element.

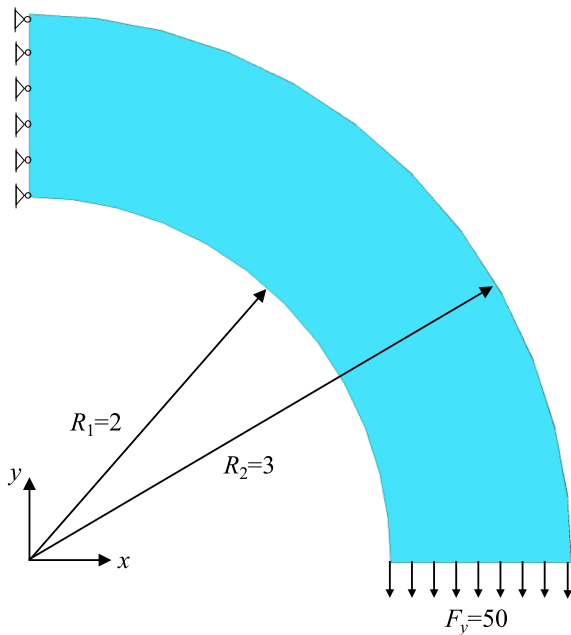


Fig. 12. Geometry description of thick-walled cylinder.

available analysis results, the mesh 2×4 scheme is considered to discretize the calculation domain, traditional mesh is shown in Fig. 4(a). And the deflection of point C is observed to compare the performance of different methods.

The distribution of mixed-order cells with two schemes is provided in Fig. 4(b) (the red lines are quadratic cells, and the blue lines represent first-order cells). When the central part of the simply supported beam is subjected to a concentrated load, a significant bending deformation will occur on the horizontal fibers, wherein high-accuracy cells are recommended. Similarly, the vertical fibers of the structure are barely bent, so almost all of them can be defined as first-order cells.

Table 3 and Fig. 5 shows the comparison of the results obtained by different approaches. The accuracy of the quadratic cells can be almost duplicated via the proposed mixed-order elements with fewer degrees of freedom. Taking scheme b as an example, the degrees of freedom are reduced by 21.6 %, and the computational deviation is only 1.3 % (detail explanations of different methods are given in Table 2, and deflection 0.4267 is considered as the exact solution, which is offered in reference (Beyabanaki et al., 2009)). Moreover, it is worth pointing out that the calculation accuracy of the proposed method is competitive, compared to the quadratic isoparametric element (Quad8).

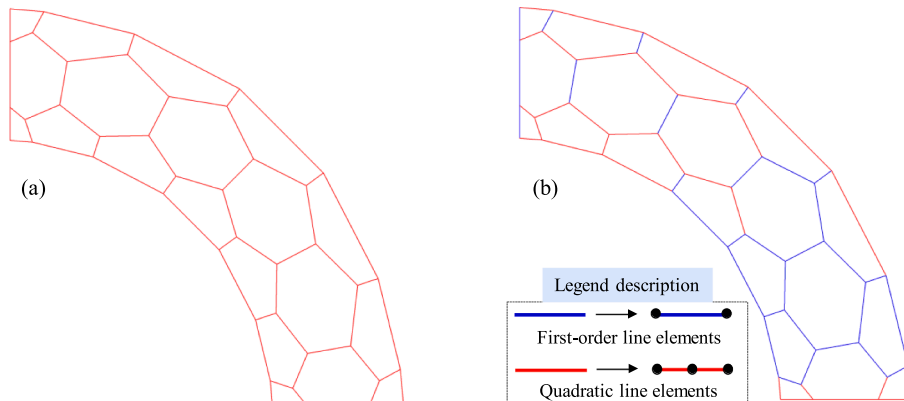


Fig. 13. Voronoi mesh of the cylinder: (a) quadratic elements, (b) mixed-order elements, $\theta = 0.5^\circ$.

3.2. A good tolerance of element distortion performance

The slender beam is shown in Fig. 6, in which different kinds of meshes are discussed, including rectangular, parallelogram and trapezoidal. The purpose of this classification is to detect the performance of the developed method for different mesh distortion factors. First, the aspect ratio is considered, then the combination of the aspect ratio and parallelogram is discussed, and third, the combination of the aspect ratio and trapezoidal distortion is inspected.

Two loading conditions are discussed in this simulation. First, transverse bending is considered, which can be defined as Load I. Load II, namely, pure bending, is also investigated. The relevant parameters are set as follows: modulus $E = 1 \times 10^7$ Pa, Poisson's ratio $\nu = 0.3$, beam thickness $t = 0.1$ m, and beam height $h = 0.2$ m. The calculated results of the end-point displacements are listed in Table 4. In addition to the presented method, the other three approaches (detail explanations are given in Table 2) are also offered for comparison.

From the results listed in Table 4, high accuracy is revealed using the presented method, while the Quad4 and QM elements suffer from mesh distortions, substantially impacting the accuracy. In other words, the method proposed in this paper has good performance to resist the mesh distortion. Especially when dealing with the trapezoidal closure problem under the condition of mesh c, the properties of high precision can continue to maintain, and even the Quad8 elements can be defeated for some conditions.

3.3. Optimized allocation of high-order boundary elements

3.3.1. Discussion of convergence and accuracy

The cook's membrane problem is the third example in this paper, and the geometric illustration is shown in Fig. 7. To better discuss the convergence and accuracy of different methods, a calculation scheme with different grid densities is set up in this paper (as shown in Fig. 8).

Transverse bending under the action of a transverse force $F = 1.0$ N is considered, and the parameters are defined according to the references, that is, the modulus $E = 1.0$ Pa and Poisson's ratio $\nu = 1/3$. Then the performance of the different elements is examined via different element types, where the quadrilateral isoparametric element is abbreviated as Quad4. Similarly, the quadratic element is defined as Quad8, SBFEM-L means that the circumferential boundaries are interpolated using a linear function, and SBFEM-Q is interpolated via a quadratic function. And the deflection of point C is observed to compare the performance of different methods. The results are listed in Table 5. Two conclusions can be drawn as follows:

- 1) The convergence and accuracy of the SBFEM is better than that of the FEM (see Fig. 9).

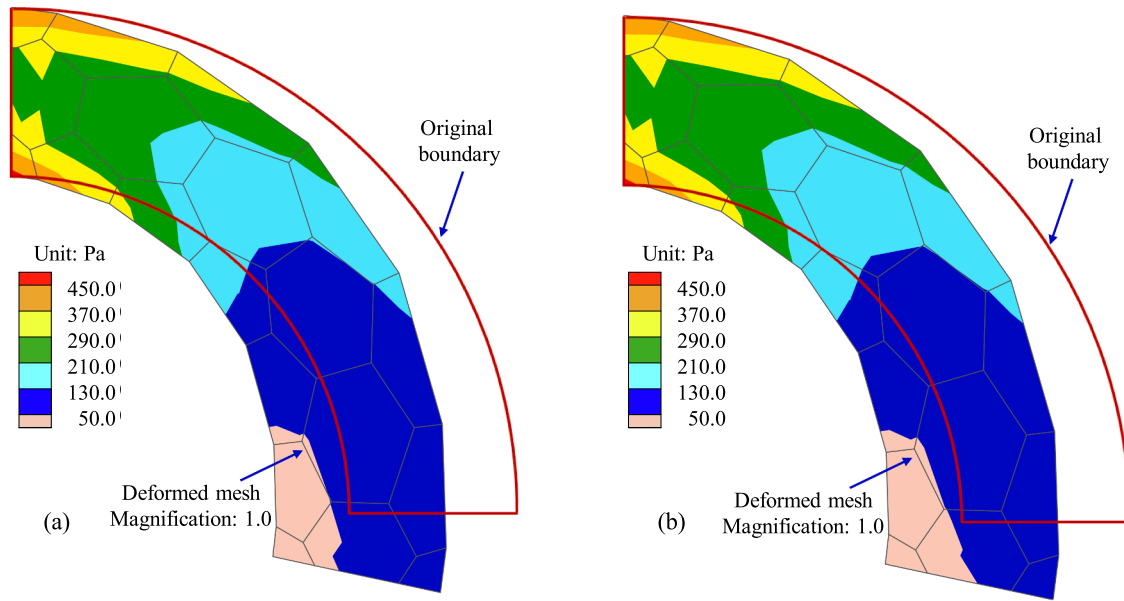


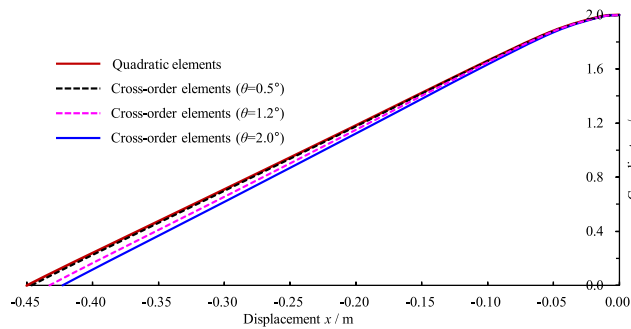
Fig. 14. Distribution of Von Mises stress: (a) quadratic elements, (b) mixed-order elements, $\theta = 0.5^\circ$.

2) For bending problems, the first-order interpolation requires more cells to approximate the analytical solution, while it can be simulated with high accuracy via the quadratic formula with fewer cells. However, more degrees of freedom are indispensable (the degrees of freedom are listed in Table 6), leading to significant reduction of computational efficiency.

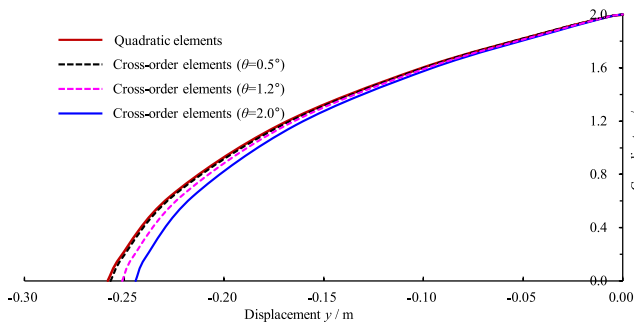
3.3.2. Optimized allocation of high-order elements

SBFEM-C represents the mixed-order SBFEM, meaning that the

boundaries are calculated through linear and quadratic functions. The advantage of mixed-order cells is that different orders of boundary elements can be reasonably selected for calculation according to requirements, thus simultaneously achieving the dual goals of high accuracy and high efficiency. However, there is no criterion to accurately discriminate and achieve the automatic assignment of elements order. In this paper, the index of deflection angle θ is introduced for the second-order elements, as shown in Fig. 10. The specific ideas are described as follows: the deformations emerged when the structure suffered from forces, and if the deflection angle of each boundary is less

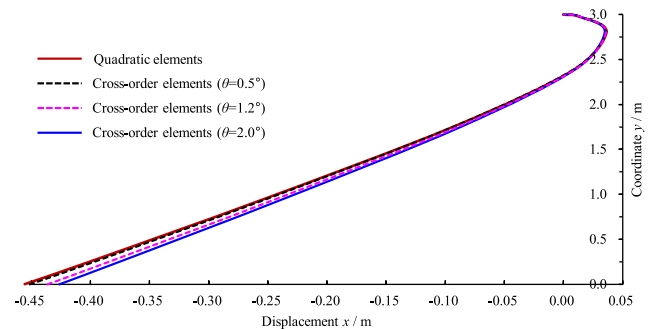


(a) displacement along x-direction

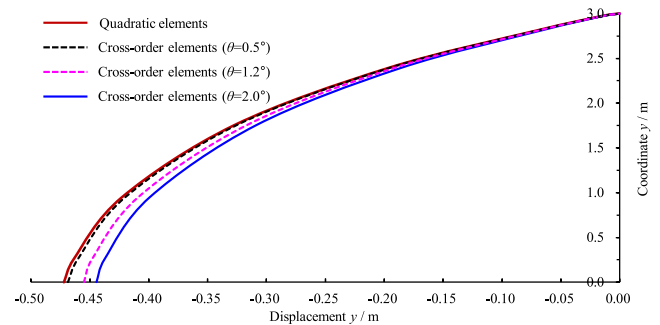


(b) displacement along y-direction

Fig. 15. Displacement distribution of the points on the inner side of cylinder ($R = 2$).



(a) displacement along x-direction



(b) displacement along y-direction

Fig. 16. Displacement distribution of the points on the outer side of cylinder ($R = 3$).

Table 8
Statistics of the maximum displacement and degrees of freedom of SBFEM-C.

Deflection angle $\theta/^\circ$	Points on inner side of cylinder with $R = 2$ (Deviation)		Points on outer side of cylinder with $R = 3$ (Deviation)		Degrees of freedom	Reduction over quadratic cells / %
	D_x / m	D_y / m	D_x / m	D_y / m		
0.0	-0.450	-0.258	-0.456	-0.472	206	–
0.5	-0.446	-0.257	-0.451	-0.468	144	30.1
	(0.9 %)	(0.4 %)	(1.1 %)	(0.8 %)		
1.2	-0.433	-0.251	-0.436	-0.455	112	45.6
	(3.8 %)	(2.7 %)	(4.4 %)	(3.6 %)		
2.0	-0.423	-0.244	-0.426	-0.444	94	54.4
	(6.0 %)	(5.4 %)	(6.6 %)	(5.9 %)		

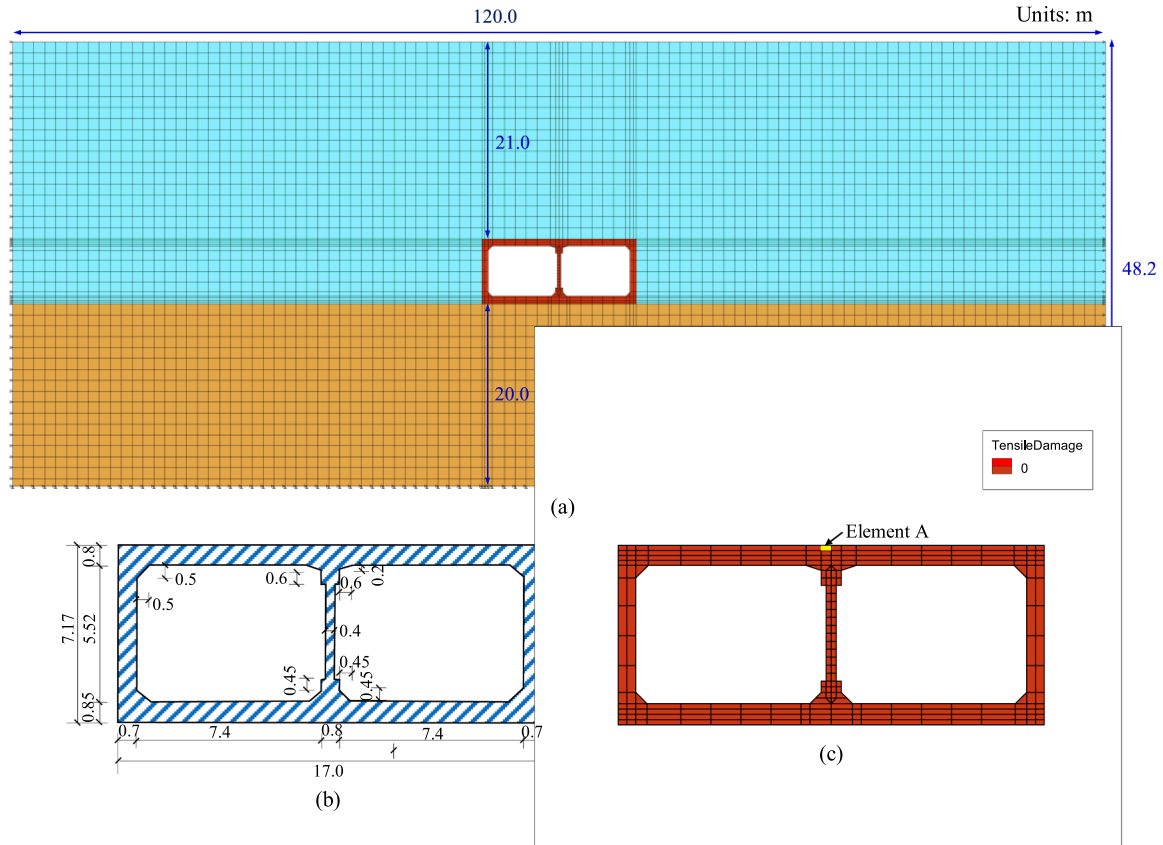


Fig. 17. Geometry and grid description of subway structures (units: m): (a) overall mesh and dimensions, (b) description of the metro geometry, (c) metro mesh.

Table 9
Parameters of the generalized plasticity model.

G_0	K_0	M_g	M_f	α_f	α_g	H_{u0}	H_{l0}	m_v
965	1288	1.68	1.30	0.10	-0.4	1100	550	0.23
m_l	m_s	β_0	β_1	γ_{DM}	r_d	γ_u	m_u	
0.45	0.23	20	0.02	20	110	5	0.45	

Table 10
Parameters of the generalized plastic interface model.

D_{s0}/kPa	D_{n0}/kPa	M_c	e_r	λ	$a/\text{kPa}^{0.5}$	b	c
1000	1500	0.88	0.0	0.091	224	0.06	3.0
γ_d	k_m	M_f	k	H_0/kPa	f_h	t/m	a
0.2	0.6	0.65	0.5	8500	2.0	0.1	0.65

than a given threshold, then the boundary element can be modified to linear interpolation. In this manner, the function of assigning elements of different orders at different accuracy locations can be materialized.

Based on the aforementioned principles, the cook's problem is recalculated adopting the discretization scheme of 8×8 in Fig. 8. To better demonstrate the characteristics of the proposed method, a schematic illustration of the mesh calculated using mixed-order cells is given in Fig. 11. For an SBFEM cell, the circumferential boundaries are marked with blue, meaning the first-order line function is adopted for interpolation, while the quadratic line elements are marked with red. By adopting this scheme, some unnecessary calculations are effectively reduced, then making the efficiency improved. As shown in Table 7, the influence of various deflection angles is explored, compared with the quadratic cells, when the computational efforts reduced by 17.3 %, the accuracy can be remained constant. And when the computational efforts reduced by 37.8 %, the accuracy is reduced by only 1.0 %. In this manner, an appropriate mixed-order scheme can be customized

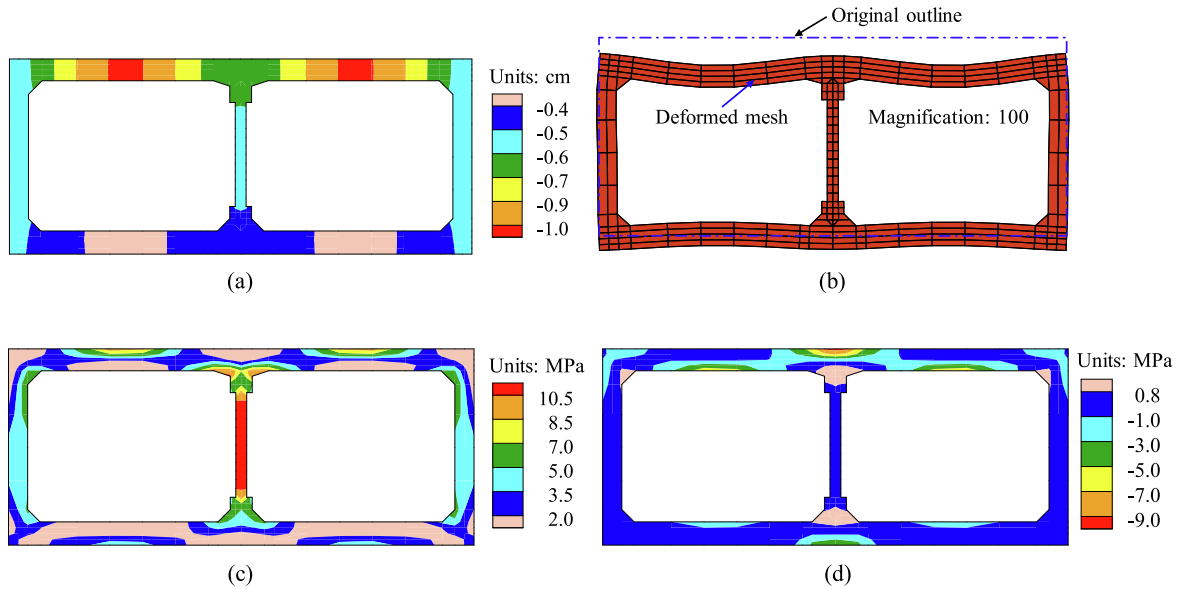


Fig. 18. Deformation and stress distribution of the subway structure: (a) vertical displacement, (b) deformed mesh, (c) major principal stress, (d) minor principal stress. (Negative values represent the tensile stress).

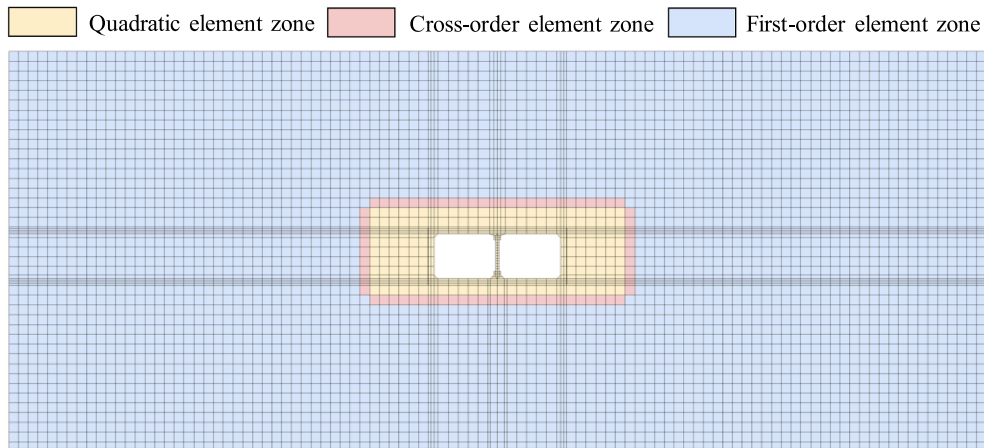


Fig. 19. The allocation schematic of elements of different orders.

according to the practical demands of researchers. In summary, it can be considered that the computational efficiency can be improved significantly without compromising the accuracy via the proposed method.

3.4. Flexible polygonal mixed-order elements

Compared with the conventional mixed-order cell, such as serendipity elements, the advantages of the scaled boundary finite element method have been inherited in the proposed method, making the polygonal mixed-order cells can be solved directly, where the flexibility of mesh discretization can be improved significantly. And the rationality can be verified via the following example.

A quarter of a thick-walled cylinder is subjected to a traction load $F_y = 50$ at its lower edge, as illustrated in Fig. 12. The inner and outer radius of cylinder are $R_1 = 2$ and $R_2 = 3$, separately. The boundary condition is fixed at left side in x-direction and y-direction. The linear elastic model is employed, and elastic modulus $E = 10000$, Poisson's ratio $\nu = 0.3$.

In Fig. 13(a), the Voronoi meshes of the cylinder are provided, and quadratic element is employed, where 103 nodes and 20 elements are

generated. To better demonstrate the properties of mixed-order cells, three schemes are considered in this simulation with different deflection angle, and in Fig. 13(b), the illustration of typical mixed-order elements are offered with deflection angle $\theta = 0.5^\circ$, in which 72 nodes are included. Compared with the quadratic elements, there are 30.1 % reduction in the number of nodes.

The Von Mises stress is provided in Fig. 14, as it can be seen, the maximum stress value and spatial distribution pattern obtained from quadratic elements can be almost duplicated via the proposed mixed-order elements.

And the displacement components of the points on the inner and outer side of cylinder, are offered in Fig. 15 and Fig. 16, where the maximum displacement values are listed in Table 8. For the purposes of comparison, the results derived from the quadratic elements, namely, the deflection angle θ is 0.0° , are determined as the reference solution. Then as the table shown, as the deflection angle θ increases, the more degrees of freedom are reduced, however, the accuracy tends to be decreased. For instance, for the scheme of $\theta = 0.5^\circ$, the degrees of freedom can be reduced by 30.1 %, the accuracy can be maintained at a satisfactory gradation, specifically, for the points on the inner side of the

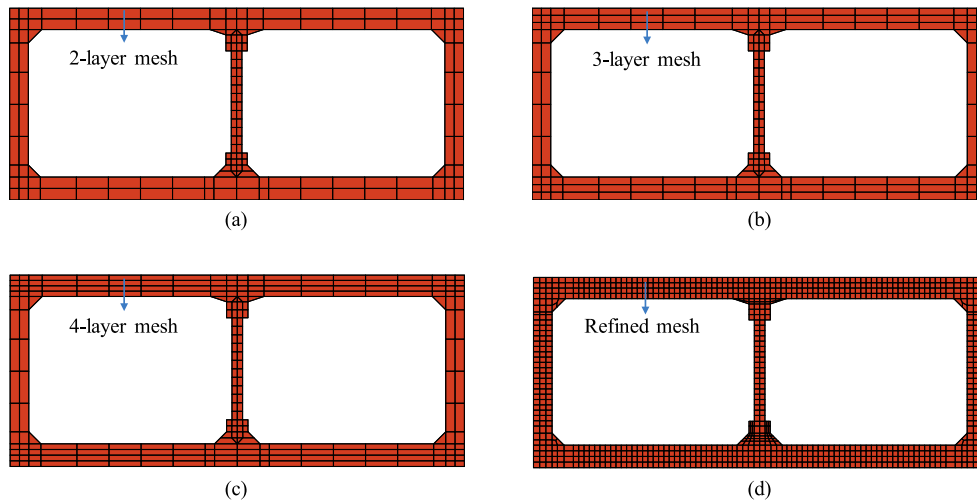


Fig. 20. Schematic of different meshes for the metro structure.

Table 11

Minor principal stress of element A for the metro structure.

Mesh	Minor principal stress / MPa (Deviation)		
	Quad4	Quad8	SBFEM-C (Presented method)
(a)	5.4 (46.5 %)	7.1 (29.7 %)	7.1 (29.7 %)
(b)	6.9 (31.7 %)	8.9 (11.9 %)	8.9 (11.9 %)
(c)	7.8 (22.8 %)	9.9 (1.98 %)	9.9 (1.98 %)
(d)	9.8 (3.0 %)	10.1	–

Table 12

Degrees of freedom for the problem.

Mesh	Degrees of freedom		Reduction over quadratic cells / %
	Quad8	SBFEM-C (Presented method)	
(a)	29,366	11,738	60.0
(b)	30,662	12,442	59.4
(c)	31,958	13,146	58.9
(d)	35,270	–	–

cylinder, only 0.9 % reduction in displacement of x-direction and 0.4 % reduction in displacement of y-direction. For the points on the outer side, the accuracy reduced by 1.1 % and 0.8 %, respectively. In summary, the computational accuracy of the proposed method is adjustable according to different analytical requirements, meanwhile, the large computational effort can be circumvented.

3.5. Application of underground engineering

To demonstrate the practicality of the proposed method in engineering, the static mechanical response of an underground structure is simulated via the software GEODYNA7.0 in this section. The bottom of the concrete subway structure is located on a rocky foundation, and on the top, there is an overlying soil layer with a height of 21.0 m. The geometry and typical grids of subway structures are provided in Fig. 17. In this analysis, a generalized plastic model is used for the overlying soil, and the parameters are listed in Table 9, in which the parameters are

obtained according to the soil distribution and experimental and simulation data provided by the literature (Chen et al., 2019). A linear elastic model is employed for the concrete and rocky foundation. To simulate the soil-structure interaction, joint elements are introduced between the concrete and the soil. Furthermore, a generalized plastic contact surface model is adopted (Liu et al., 2014), and the parameters are listed in Table 10.

As shown in Fig. 18, the deformation and stress distribution are obtained from the quadratic elements. As seen, the top of the subway structure will experience vertical downward settlement deformation due to the gravitational effect of the overlying soil, while there are supporting roles generated from the central concrete column. This makes uneven bending deformation occur on the top concrete, namely, the deformation pattern illustrated in Fig. 18(b). Under this deformation, a large tensile stress appears in the top concrete, of which the maximum value (9.9 MPa) is measured from element A, which is located at the top of the central column (see in Fig. 17(c)).

As previously mentioned, more accurate results can be obtained using the quadratic elements for the bending deformation effect of the structure. Therefore, in this simulation, according to the deformation pattern of the underground structure, the quadratic elements are selected for managing the local area, and the first-order elements are adopted for the soil zone, which dominates the majority of the area. The coordination at the junction is achieved by the proposed mixed-order elements, and a schematic description is illustrated in Fig. 19. Moreover, since there is no theoretical solution to the problem, meshes of different numbers of layers of elements for the top and bottom concrete are considered, and the illustration is provided in Fig. 20. Subsequently, based on the abovementioned conditions, the force characteristics of the structure are further analyzed.

The results obtained from different grids are listed in Table 12, and since there is no theoretical solution to the problem, mesh (d) is adopted for the reference solution, then the error can be calculated using Eq. (21).

$$\text{Error} = (10.1 - \sigma_{(i)}) / 10.1 \times 100\%, \quad i = a, b, c$$

The shear lock phenomenon inevitably occurs when quadrilateral elements are used to solve the bending deformation. Generally, the problem can be alleviated using approaches with a higher accuracy, such as quadratic elements or nonconforming elements. According to the results in Table 11, a satisfactory accuracy can be achieved via the presented mixed-order elements, which can duplicate the effectiveness of quadratic elements, and moreover, compared to the quadratic elements, 58.9 % computational freedom can be eliminated with a relative

deviation of 1.98 % via the mixed-order elements (see Table 12). In doing so, it can be believed that the computational efficiency can be optimized markedly.

4. Conclusion

In this paper, based on SBFEM theory, a flexible and versatile mixed-order approach is developed, wherein the circumferential boundaries are interpolated via one-dimensional linear and quadratic functions; subsequently, the applicability and solution accuracy to different problems are explored and compared. The main conclusions are summarized as follows:

- (1) A good accuracy and performance against cells distortion are revealed in the proposed method. Through two classical arithmetic examples, it is shown that the accuracy of the proposed method is impressive compared with other methods. Moreover, the performance against cell distortion is improved for different problems, indicating the accuracy and robustness are enhanced for representative meshes.
- (2) Compared with the quadratic elements, the computational costs are markedly reduced via the proposed method, enabling the efficiency to be improved. The precise locations of higher-order boundary cells are allocated according to the presented index of deflection angle, in this manner, the optimized computational resources can be achieved, resulting in the computational efforts can be decreased by 17.3 % without compromising the accuracy for representative meshes.
- (3) More flexibility and versatility are attained with the proposed method. Compared with the commonly used serendipity mixed-order elements, polygonal mixed-order cells can be calculated directly, wherein satisfactory universalities are revealed, and the advantages can be further amplified when processing complex geometries.

The proposed method can be easily extended to three-dimensional applications and will be able to demonstrate its superiority preferably, which is also our primary focus in future research.

CRedit authorship contribution statement

Kai Chen: Conceptualization, Writing – original draft, Software, Formal analysis. **Degao Zou:** Conceptualization, Software, Writing – review & editing. **Jingmao Liu:** Writing – review & editing. **Yue Zhuo:** Validation.

Declaration of Competing Interest

The authors declare that they have no known competing financial interests or personal relationships that could have appeared to influence the work reported in this paper.

Data availability

No data was used for the research described in the article.

Acknowledgements

This work was supported by the National Natural Science Foundation of China (Grant Nos. 52192674, U1965206, 52009018) and the Fundamental Research Funds for the Central Universities (Grant Nos. DUT21RC(3)099).

References

- Aylor, R.L., Beresford, P.J., Wilson, E.L., 2010. A non-conforming element for stress analysis. *Int. J. Numer. Meth. Eng.* 10 (6), 1211–1219.
- Beyabanaki, S.A.R., Jafari, A., Biabanaki, S.O.R., et al., 2009. Nodal-based three-dimensional discontinuous deformation analysis (3-D DDA). *Comput. Geotech.* 36 (3), 359–372.
- Birk, C., Behnke, R., 2012. A modified scaled boundary finite element method for three-dimensional dynamic soil-structure interaction in layered soil. *Int. J. Numer. Meth. Eng.* 89 (3), 371–402.
- Carey, G.F., Olsen, J.T., Saunders, H., 1987. *Finite Elements—A Second Course* (Vol. II).
- Chen, D., Birk, C., Song, C., et al., 2014. A high-order approach for modelling transient wave propagation problems using the scaled boundary finite element method. *Int. J. Numer. Meth. Eng.* 97 (13), 937–959.
- Chen, Y.F., Zeng, J., Shi, H., et al., 2021b. Variation in hydraulic conductivity of fractured rocks at a dam foundation during operation. *J. Rock Mech. Geotech. Eng.* 13 (2), 351–367.
- Chen, K., Zou, D.G., Kong, X.J., 2017. A nonlinear approach for the three-dimensional polyhedron scaled boundary finite element method and its verification using Koyna gravity dam. *Soil Dyn. Earthq. Eng.* 96, 1–12.
- Chen, K., Zou, D.G., Kong, X.J., et al., 2018a. Global concurrent cross-scale nonlinear analysis approach of complex CFRD systems considering dynamic impervious panel-rockfill material-foundation interactions. *Soil Dyn. Earthq. Eng.* 114, 51–68.
- Chen, K., Zou, D.G., Kong, X.J., et al., 2018b. An efficient nonlinear octree SBFEM and its application to complicated geotechnical structures. *Comput. Geotech.* 96, 226–245.
- Chen, K., Zou, D.G., Kong, X.J., et al., 2019. Elasto-plastic fine-scale damage failure analysis of metro structures based on coupled SBFEM-FEM. *Comput. Geotech.* 108, 280–294.
- Chen, K., Zou, D.G., Tang, H.X., et al., 2021a. Scaled boundary polygon formula for Cosserat continuum and its verification. *Eng. Anal. Bound. Elem.* 126, 136–150.
- Çitipitioglu, E., 1983. Universal serendipity elements. *Int. J. Numer. Meth. Eng.* 19 (6), 803–810.
- Droniou, J., Eymard, R., Gallouët, T., et al., 2021. Non-conforming finite elements on polytopal meshes. In: *Polyhedral Methods in Geosciences*. Springer, Cham, pp. 1–35.
- Egger, A., Pillai, U., Agathos, K., et al., 2019. Discrete and phase field methods for linear elastic fracture mechanics: a comparative study and state-of-the-art review. *Appl. Sci.* 9 (12), 2436.
- Gopalakrishnan, R., Vijayakar, S., Busby, H., 1990. An iterative algorithm for adaptive element splitting using transition elements. *Comput. Struct.* 37 (3), 283–294.
- Gravenkamp, H., Saputra, A.A., Song, C.M., et al., 2017. Efficient wave propagation simulation on quadtree meshes using SBFEM with reduced modal basis. *Int. J. Numer. Meth. Eng.* 110 (12), 1119–1141.
- Guo, N., Yang, Z., Yuan, W., et al., 2021. A coupled SPFEM/DEM approach for multiscale modeling of large-deformation geomechanical problems. *Int. J. Numer. Anal. Meth. Geomech.* 45 (5), 648–667.
- Honarmand, M., Moradi, M., 2018. Scaled boundary finite element simulation and modeling of the mechanical behavior of cracked nanographene sheets. *Superlattice. Microsc.* 118, 242–255.
- Huang, Y., Yang, Z., Ren, W., et al., 2015. 3D meso-scale fracture modelling and validation of concrete based on in-situ X-ray Computed Tomography images using damage plasticity model. *Int. J. Solids Struct.* 67, 340–352.
- Huang, Z., Zheng, H., Guo, L., et al., 2020. Influence of the position of artificial boundary on computation accuracy of conjugated infinite element for a finite length cylindrical shell. *Acoustics Australia* 48 (2), 287–294.
- Li, P., Liu, J., Lin, G., et al., 2017. A NURBS-based scaled boundary finite element method for the analysis of heat conduction problems with heat fluxes and temperatures on side-faces. *Int. J. Heat Mass Transf.* 113, 764–779.
- Li, J., Shi, Z., Liu, L., 2018. A unified scaled boundary finite element method for transient two-dimensional vibro-acoustic analysis of plate-like structures. *Comput. Struct.* 202, 105–128.
- Li, J., Shi, Z., Liu, L., et al., 2020. An efficient scaled boundary finite element method for transient vibro-acoustic analysis of plates and shells. *Comput. Struct.* 231, 106211.
- Liu, J., Ye, W., Zang, Q., Lin, G., 2020. Deformation of laminated and sandwich cylindrical shell with covered or embedded piezoelectric layers under compression and electrical loading. *Compos. Struct.* 240, 112041.
- Liu, J., Hao, C., Ye, W., Yang, F., Lin, G., 2021a. Free vibration and transient dynamic response of functionally graded sandwich plates with power-law nonhomogeneity by the scaled boundary finite element method. *Comput. Methods Appl. Mech. Eng.* 376, 113665.
- Liu, J., Hao, C., Zhou, Y., Ye, W., 2021b. Dynamic analysis of functionally graded sandwich beams using a method named scaled finite element method. *Eng. Anal. Bound. Elem.* 130, 161–175.
- Liu, J., Ye, W., Zang, Q., Lin, G., 2022. Semianalytical piezoelectric solution of orthotropic circular cylindrical panel using SBFEM: Bending and free vibrations. *Mech. Adv. Mater. Struct.* 29 (2), 303–320.
- Liu, L., Zhang, J., Song, C., et al., 2019. An automatic approach for the acoustic analysis of three-dimensional bounded and unbounded domains by scaled boundary finite element method. *Int. J. Mech. Sci.* 151, 563–581.
- Liu, J., Zou, D., Kong, X., 2014. A three-dimensional state-dependent model of soil-structure interface for monotonic and cyclic loadings. *Comput. Geotech.* 61, 166–177.
- Nicolas, V.T., Citipitioglu, E., 1977. A general isoparametric finite element program SDRS SUPERB. *Comput. Struct.* 7 (2), 303–313.
- Ooi, E.T., Shi, M.G., Song, C.M., et al., 2013. Dynamic crack propagation simulation with scaled boundary polygon elements and automatic remeshing technique. *Eng. Fract. Mech.* 106, 1–21.

- Ooi, E.T., Natarajan, S., Song, C., et al., 2016. Dynamic fracture simulations using the scaled boundary finite element method on hybrid polygon quadtree meshes. *Int. J. Impact Eng* 90, 154–164.
- Reddy, J.N., 2004. *An introduction to the finite element method*. McGraw-Hill, New York.
- Song, C.M., 2009. The scaled boundary finite element method in structural dynamics. *Int. J. Numer. Meth. Eng.* 77 (8), 1139–1171.
- Song, C.M., 2018. *The Scaled Boundary Finite Element Method*. John Wiley & Sons Ltd, Hoboken.
- Song, C.M., Wolf, J.P., 1997. The scaled boundary finite-element method—alias consistent infinitesimal finite-element cell method—for elastodynamics. *Comput. Methods Appl. Mech. Eng.* 147 (3–4), 329–355.
- Utku, M., 1999. An improved transformation for universal serendipity elements. *Comput. Struct.* 73 (1–5), 199–206.
- Vu-Huu, T., Le-Thanh, C., Nguyen-Xuan, H., et al., 2019. A high-order mixed polygonal finite element for incompressible Stokes flow analysis. *Comput. Methods Appl. Mech. Eng.* 356, 175–198.
- Wolf, J.P., 2003. *The scaled boundary finite element method*. John Wiley & Sons.
- Wriggers, P., Hudobivnik, B., Aldakheel, F., 2021. NURBS-based geometries: A mapping approach for virtual serendipity elements. *Comput. Methods Appl. Mech. Eng.* 378, 113732.
- Xu, B., Zou, D., Kong, X., et al., 2015. Dynamic damage evaluation on the slabs of the concrete faced rockfill dam with the plastic-damage model. *Comput. Geotech.* 65, 258–265.
- Xu, H., Zou, D., Kong, X., et al., 2016. Study on the effects of hydrodynamic pressure on the dynamic stresses in slabs of high CFRD based on the scaled boundary finite-element method. *Soil Dyn. Earthq. Eng.* 88, 223–236.
- Yang, Z., Ren, W., Sharma, R., et al., 2017. In-situ X-ray computed tomography characterisation of 3D fracture evolution and image-based numerical homogenisation of concrete. *Cem. Concr. Compos.* 75, 74–83.
- Zhao, J., Chen, S., Zhang, B., 2016. The nonconforming virtual element method for plate bending problems. *Math. Models Methods Appl. Sci.* 26 (09), 1671–1687.
- Zhao, S., Zhao, J., 2019. A poly-superellipsoid-based approach on particle morphology for DEM modeling of granular media. *Int. J. Numer. Anal. Meth. Geomech.* 43 (13), 2147–2169.
- Zhao, S., Zhao, J., Lai, Y., 2020. Multiscale modeling of thermo-mechanical responses of granular materials: A hierarchical continuum–discrete coupling approach. *Comput. Methods Appl. Mech. Eng.* 367, 113100.
- Zou, D.G., Chen, K., Kong, X., et al., 2017. An enhanced octree polyhedral scaled boundary finite element method and its applications in structure analysis. *Eng. Anal. Bound. Elem.* 84, 87–107.
- Zou, D.G., Teng, X., Chen, K., et al., 2019. A polyhedral scaled boundary finite element method for three-dimensional dynamic analysis of saturated porous media. *Eng. Anal. Bound. Elem.* 101, 343–359.